ISTANBUL TECHNICAL UNIVERSITY ★ GRADUATE SCHOOL

QUANTITATIVE HOLOGRAPHIC MICROWAVE IMAGING WITH A SIMULATED CALIBRATION MEASUREMENT

M.Sc. THESIS

Ahmet Caner GÜL

Department of Electronics and Communication Engineering

Telecommunications Engineering Programme

JANUARY 2025

ISTANBUL TECHNICAL UNIVERSITY ★ GRADUATE SCHOOL

QUANTITATIVE HOLOGRAPHIC MICROWAVE IMAGING WITH A SIMULATED CALIBRATION MEASUREMENT

M.Sc. THESIS

Ahmet Caner GÜL
(504221301)

Department of Electronics and Communication Engineering

Telecommunications Engineering Programme

Thesis Advisor: Asst. Prof. Dr. Semih DOĞU

JANUARY 2025

İSTANBUL TEKNİK ÜNİVERSİTESİ ★ LİSANSÜSTÜ EĞİTİM ENSTİTÜSÜ

SİMÜLASYON İLE ELDE EDİLEN KALİBRASYON ÖLÇÜMLERİ ÜZERİNDEN NİCEL MİKRODALGA HOLOGRAFİ YÖNTEMİ

YÜKSEK LİSANS TEZİ

Ahmet Caner GÜL
(504221301)

Elektronik ve Haberleşme Mühendisliği Anabilim Dalı

Telekomünikasyon Mühendisliği Programı

Tez Danışmanı: Dr. Öğr. Üyesi Semih DOĞU

OCAK 2025

Ahmet Caner GÜL, a M.Sc. student of ITU Graduate School student ID 504221301 successfully defended the thesis entitled "QUANTITATIVE HOLOGRAPHIC MICROWAVE IMAGING WITH A SIMULATED CALIBRATION MEASUREMENT", which he prepared after fulfilling the requirements specified in the associated legislations, before the jury whose signatures are below.

Thesis Advisor : **Asst. Prof. Dr. Semih DOĞU** ....
Istanbul Technical University

Jury Members : **Assoc. Prof. Dr. Mehmet Nuri AKINCI** ....
Istanbul Technical University

Asst. Prof. Dr. Egemen BİLGİN ....
MEF University

Date of Submission : **28 January 2025**
Date of Defense : **28 January 2025**

To my family

FOREWORD

I would like to express my heartfelt gratitude to my thesis advisor, Dr. Semih Doğu, for unwavering support and invaluable guidance, and to Doç. Dr. Mehmet Nuri Akıncı for providing profound expertise and insightful contributions. Their mentorship has been instrumental in shaping the direction and quality of this work.

I am also deeply thankful to my esteemed colleagues and my family for their constant encouragement and support throughout my research. This thesis supported by İTÜ BAP under Grant Number MYL-2024-45595.

January 2025

Ahmet Caner GÜL
(Research Assistant)

TABLE OF CONTENTS

Page

ABBREVIATIONS

QMH : Quantitative Microwave Holography
PSF : Point Spread Function
CO : Calibration Object
RO : Reference Object
OUT : Object Under Test
PS : Point Scatterer
VIE : Volume Integral Equation
CS : Compressed Sensing
LSM : Linear Sampling Method
FM : Factorization Method
NOSM : Near Orthogonal Sampling Method
CSI : Contrast Source Inversion
TSVD : Truncated Singular Value Decomposition

SYMBOLS

ε_r : Relative dielectric permittivity
μ_r : Relative dielectric permeability
λ : Wavelength
χ : Normalized contrast function
Ω : Object domain
ω : Radial frequency
γ : Born condition number
ζ : Indice of transmitter-receiver pair
K : Kernel of scattering integral
κ : Spectral space
δ_i : Resolution of the i'th axis

LIST OF FIGURES

QUANTITATIVE HOLOGRAPHIC MICROWAVE IMAGING WITH A SIMULATED CALIBRATION MEASUREMENT

SUMMARY

Microwave imaging is a new technology that has recently been introduced into use. This imaging technology can be applicable in various fields, including medical examination and tumor detection, material characterization, foreign object detection, security applications, and many other areas, owing to their effectiveness in the near field and their non-ionizing properties.

Microwave imaging is fundamentally based on solving the inverse scattering problem and numerous techniques for solution have been proposed and studied in the literature. Due to the ill-posed nature of the problem, the non-unique solution is the main issue and restricts our ability to find the exact parameters of objects in the results. Therefore, these techniques can be divided into two main categories based on the results obtained: qualitative and quantitative. While qualitative results provide only the contrast value of an object due to limited system definitions and prioritization of faster results, quantitative methods yield the actual value of the object by sacrificing the calculation speed and generalization in imaging calculations. The Holographic Imaging technique is one of the promising methods that offers quantitative and faster results but in return, it requires precise calibration procedures customized to the environment.

In this thesis, the recently proposed Quantitative Microwave Holography (QMH) method is applied in dielectric imaging and the technique has improved by means of its calibration time drawback. The general QMH algorithm is more generalizable to object shapes compared to other quantitative techniques but not the object's actual values, and it needs to calibration to both environment and possible dielectric parameters space to get attainable results.

This technique gives 3D quantitative results by basically using system response or system function obtained from the calibration procedure and using spectral reconstruction technique with the aid of linearization and holography. It is possible by inverting the convolution of this system function and the contrast function in the spectral domain after applying linearization to the famous non-linear scattering equation. The transfer function of the system is obtained by finding the scattering response of the point scatterer (PS) in each slant range position and this process is applied in each range space for the regular QMH method. Once the system response is determined, the object under test (OUT) response is obtained and the object function is resolved using regularization methods, such as Tiknhonov regularization, from the linear system where these two scattering data are related in the spectral domain by a product. The linear system that is used in the resolving step, is obtained using linearization approximations such as Born and Rytov. The Born and Rytov

approximations are general methods that assume there are no internal scatterings or there are constant phase characteristics in objects respectively. Due to these assumptions, the object being imaged or CO being used has to be of limited size or have limited contrast values where these two requirements are drawbacks of QMH algorithm. All the scattering data used in reconstruction is obtained by subtracting the background information according to the Holography technique to obtain the difference data as in optical holography and this is the reason why we called this imaging method holographic imaging.

In our proposed method, this time-consuming calibration procedure in the real world is replaced by a simulation environment. With this approach calibration procedure will be accelerated and some drawbacks of real measurement-based calibration procedures such as clutter noise from the background or issues with non-stable device characteristics will be eliminated by the ideal simulation. To utilize the simulation approach in such a precise calibration procedure, there has to be an identical simulation environment. Owing to the holography technique, stationary background properties are eliminated by subtracting operation and there is only the remaining modeling antenna system itself in the ideal case. The second part of this thesis consists of modeling the antenna system and this modeling is done by using Volume Integral Equation (VIE). In this method, the field of the identically modeled receiver antenna is used instead of the system Green function. However, this obtained field from the simulation environment has to be equated with the value in the real measurement setup. Therefore one calibration data measured from real real-world setup is used for normalization. In this way, only one measurement for all calibration procedures will be required and calibration procedure time will be equal to the processing time of computer speed.

SİMÜLASYON İLE ELDE EDİLEN KALİBRASYON ÖLÇÜMLERİ ÜZERİNDEN NİCEL MİKRODALGA HOLOGRAFİ YÖNTEMİ

ÖZET

Uzaktan algılama ve görüntüleme teknikleri arasında son dönemde gelişim gösteren mikrodalga görüntüleme tekniği elde edilen görüntünün kalitesinin iyileştirilmesinde ve geleneksel görüntülemede kullanılan zararlı radyasyonun ortadan kaldırılmasını sağlayarak yenilikçi bir çözüm sunmaktadır. Bu sayede, özellikle tıbbi görüntüleme gibi detaylı ve çok sayıda görüntüleme ihtiyacı olan alanlarda kullanım potansiyeli oldukça yüksektir. Ayrıca geçmişten günümüze kullanımı yaygın olan X-ray tarayıcılarının çalışma tekniğine kıyasla daha ucuz bir tarama sonucu elde edilebilme imkanı da bulunabilmekte ve iyonize olmayan bir radyasyon çeşidi olduğundan X-ray taramanın sağlığa verdiği zararı ortadan kaldırmaktadır. Gerçek hayatta elektromanyetik görüntüleme güvenlikte, askeriyede, tıbbi görüntülemede, havacılık ölçme vb. akla gelebilecek uygulama alanlarında kullanım imkânı bulmaktadır. Uygulama alanlarına örnek olarak, optik dalga boylarında tespiti sağlanamayan ve infrared izi bulunmayan fakat mikrodalga boylarının geçebildiği yüzeyler arkasına gizlenmiş obje tespiti, gizlenmiş olan silah gibi objeler giysi arkasından görüntülenmesi gibi uygulamalar örnek verilebilir. Sağlık alanında ise tıbbi görüntülemede kanserli doku teşhisinde veya diğer vücut dokularının görüntülenmesidir. Ayrıca gıdaların analizinde, kalite kontrolünde ve üretim hattında yabancı cisimlerin tespitinde mikrodalga görüntüleme teknolojisinden faydalanılabilir.

Mikrodalga görüntüleme sistemleri, görüntülenmek istenen cismin bulunduğu hedef bölgeden saçılan elektromanyetik dalgaları kullanarak ilgili hedefin elektriksel parametrelerini ve bu parametrelerin konumsal bilgisini ters saçılım problemi üzerinden elde ederek hedefin görüntüsünü çıkarmayı hedeflemektedir. Buradaki problem doğası gereği kötü konumlandırılmış lineer olmayan bir denklem olarak ortaya çıkmakta ve çözümü tek olmayarak birden fazla şekilde oluşturulabilmektedir. Bu tekil olmayan çözümler bizim problemimizin ana kaynağını oluşturmaktadır ve çözüm yetkinliğimizi kısıtlamaktadır. Yine bu kısıtlama sebebiyle elde edeceğimiz sonuçlar gerçek değerler veya sadece fark değerleri olarak ortaya çıkmaktadır. Ters problemden elde edilen bu değerlere göre sonuçlar, nicel (doğrudan elektriksel parametrelerin değerini tayin eden) veya nitel (elektriksel parametre bulmaksızın sadece saçıcının şeklini bulmaya odaklanan metotlar) olarak sınıflandırılabilmektedir. Kullanılacak yöntemler de sonucun nicel/kantitatif veya nitel/kalitatif olmasına göre çeşitli yaklaşımlar altında çözüm elde etmeyi amaçlamaktadır. Genel olarak, kantitatif yaklaşımla sonuç elde etmeyi amaçlayan yöntemler hızlı sonuç ile yalnızca kontrast değeri bulmayı hedeflerken; nitel yöntemler hızdan ödün vererek gerçek değeri elde etmeyi amaçlamaktadır. Nitel yöntemler daha çok iteratif yollarla gerçek

sonuca yakınsamaya çalışırken, nicel yöntemler yukarıda bahsettiğimiz bu lineer olmayan denklemi doğruluktan taviz vererek önce lineerleştirip tek bir adımda çözümü hedeflemektedir. Bu yöntemlerden biri olan Holografik Görüntüleme metodu hızlı şekilde nitel veya nicel sonuç verebilen etkili bir yöntem olarak karşımıza çıkmakta. Holografi metodu diğer nitel yöntemlere kıyasla hedef nesnenin şekline daha az duyarlı olurken, elektriksel parametrelerine daha duyarlıdır. Bu sebeple daha doğru nicel sonuçlar veya doğrudan nitel sonuçlar elde etmek için hedef cisme yakın elektriksel özelliklere sahip bir referans cisim ile hassas kalibrasyon işlemine ihtiyaç duymaktadır.

Bu tez kapsamında Nicel Holografik Mikrodalga görüntüleme tekniği dielektrik maddelerin görüntülenmesinde test edilmiş ve kullanılan kalibrasyon metodu simülasyon ortamı sayesinde hızlandırılmaya çalışılmıştır. Bu metot temelde, lineerleştirme ve holografi metotlarını birlikte kullanarak, kalibrasyon üzerinden elde edilen sistem yanıtı ve cisme ait saçılma parametrelerini üzerinden spektral düzlemde görüntü elde etmeyi amaçlamaktadır. Burada elde edilen görüntü kontrast fonksiyonun bir fonksiyonudur ve bu kontrast fonksiyonu lineerleştirilmiş sistem yanıtının konvolüsyonu ile saçılma verisini vermektedir. Bu konvolüsyon işlemi ters saçılım problemini denkleminden gelmekte olup spektral düzlemde lineer ters işlemle çözümü sayesinde hedef nesneye ait aranan kontrast fonksiyonunu vermektedir. Bu sistem yanıtı veya başka bir deyişle sistem fonksiyonu, nokta saçıcıya ait saçılma verisinin uzayın her bir kesite ait düzlemdeki her noktasında ölçümüne ve sistemin bu ölçüme göre düzenlenmesiyle veya kalibre edilmesiyle elde edilmektedir. Bu kalibrasyonda kullanılan nokta saçıcı daha önceden elektriksel parametreleri bilinen boyutları birim saçıcıya denk düşecek bir referans nesne üzerinden gerçekleştirilmektedir. Elde edilen nokta saçıcıya ait s-parametreleri üzerinden holografi metoduna göre arka plan saçılımı çıkarılmasıyla sisteme ait tepki yanıtı bulunmuş olunur. Buradaki holografi tekniği optik holografi tekniğinden farksızdır. Yöntemde kullanılan lineerleştirme işlemi ise Born veya Rytov adı verilen iki farklı tekniğin uygulanması ile gerçekleştirilmektedir. Born yaklaşımı adı verilen bu teknik nesne içerisindeki iç saçılımların ihmali yaklaşımını kullanırken, Rytov yaklaşımı nesnenin içinden geçen dalganın fazındaki değişiminin çok küçük değerlerde olduğu yaklaşımını kullanır. Her iki yaklaşımın da geçerli olabilmesi için objenin boyutlarına ve elektriksel özelliklerine ait çeşitli kısıtlamalar bulunmaktadır. Bu da nicel mikrodalga görüntülemenin bir kısıtlaması olarak görülebilecek şekilde kalibrasyon objesinin (Calibration Object-CO) boyutlarına ve kontrastına belirli sınırlamalar getirmektedir.

Bu tez kapsamında önerilen metotta, gerçek ölçüm ortamında yapılan hem zaman alıcı hem de gürültü sebebiyle bozulmaya açık kalibrasyon işlemi simülasyon ortamına taşınarak daha ideal hale getirilmeye çalışılmıştır. Holografi tekniği sayesinde arka plan etkileri çıkarıldığından bu yöntemin simülasyon ortamında gerçekleştirilebilmesi için gerçek sistemin birebir modelinin dijital ortamda kopyası oluşturulması yeterlidir.

Bu kalibrasyon ölçümleri simülasyon ortamında gerçekleştirilmesine rağmen, kullanılan tam dalga çözümlerinin yavaş olması sebebiyle, ölçüm süreleri bir hayli uzun olmaktadır. Bu sorunun çözülebilmesi için tezin ikinci kısmı olan vektör integral denklemlerinin kullanılması düşünülmüştür. Bu yöntemde kontrast fonksiyonu saçıcı denklemindeki integral çekirdeği, nesne uzayına ait tek bir simülasyonla elde edilebilen elektrik alan verisinden doğrudan elde edilen vektör Green fonksiyonu ile değiştirilmiştir. Vektör Green fonksiyonu doğrudan verici antene ait elektrik alan üzerinden elde edilebildiğinden simülasyon üzerinde uzayın her noktasında ölçüm zorunluluğu ortadan kaldırılmış ve işlemin süresi kısaltılmıştır. VIE algoritması ile elde edilen sonuçların gerçek ölçümle birebir olması için algoritma üzerinde modellenen iletim hattı tek bir gerçek ölçüm üzerinden kalibre edilmiştir.

Sonuç olarak kullanılan algoritma sayesinde tek bir gerçek ölçüm verisiyle görüntüleme sistemi kalibrasyonu gerçekleştirilmiş ve holografik görüntüleme yöntemine ait kalibrasyon prosedürü hızlandırılmış ve iyileştirilmiştir.

1. INTRODUCTION

Microwave and millimeter wave imaging are emerging technologies with non-ionization radiation and simplicity in application compared to other imaging methods such as tomography, X-ray scanners, or techniques that use radio-pharmaceutical agents. Although X-ray scanners have nm-level resolutions which are better than radio imaging techniques, X-ray ionizes organic molecules and is harmful to living cells. For this reason, radio imaging is a good candidate for frequent usage. Also, with smaller circuitry in microwave technology, these systems take less area and give higher spatial resolutions. With the improvement of technologies in microwave circuit technology, higher resolutions, and more compact systems could be obtained in the future.

Radio imaging techniques give an image of the target under information on the electrical parameters of the object. It is based on, the process of collection and evaluation of the information of scattered fields from the object being illuminated by transmitted known fields. Since electrical fields can penetrate through the body and objects, they can easily get electrical information from within the targets. In the final data, obtained information will be complex and it resembles both the conductivity and permittivity or permeability of materials. In radio imaging applications, both waves passing through objects and the waves scattered from objects, which is not the case in X-ray imaging, can be used, depending on the imaging setup. In this way, the information from gathered objects will be enriched when both types of waves are used. Since it only requires one side or receiver of the system, generally only collecting the scattered field would be preferable.

Extracting these electrical parameters is based on inverse scattering solutions. Wave and material interact with each other in a forward scattering manner and are formulated by integral field equations which also contain electrical parameters under integral. This integral solved inversely by using many techniques in literature and each technique approach this inverse problem with particular assumption or take prior information to alleviate the problem. Also this problem due to it is nature, leads to ill-posed type solutions when space is discretized and to be able to solve this ill-posedness, regularization techniques, and optimization algorithms or even machine learning algorithms could be used [1–3].

1.1 Purpose Of This Thesis

In this thesis, we aim to speed up the calibration procedure, reduce noise effect and measurement errors due to scanning, and eliminate the all-space measurement need of quantitative microwave holographic imaging.

1.1.1 Usage areas of microwave imaging

In application, microwave imaging could be used in areas like other methods depicted above, such as; medical imaging, food inspection, security, and military applications. In medical applications, different tissues are targeted in imaging to detect malign cells or to use in inspection, such as breast cancers [4, 5], bone fractures [6] and even brain strokes [7] could be successfully detected without harming any health organs or tissues with the aid of radio imaging technique. In food production imaging is generally used to enhance the quality of production by extracting the good ones and rotten ones [8] and discriminating foreign objects [9] that have been mixed in the fabrication. Microwave imaging can also be used in security applications such as body scanners that detect the lethal objects hidden on people [10], or devices that are directly used to detect human existence in intrusion in-home or border security [11].

1.2 Literature Review

Microwave imaging techniques mainly aim to solve inverse source problems where the corresponding forward solution of the inverse equation is unique but the inverse is not. The Inverse scattering problem has an ill-posed nature due to the limited conditions of the real-world environment, and it leads to an optimization problem that can be solved by using the forward equation iteratively or applying linearization methods [12]. In both cases, some pre-known information is required to enhance the solution system, and a solution method is needed that either reduces the equation to the simple form or uses a system of equations that is constructed with frequency or spatial sampling data to improve optimization conditions [13]. These problems can be divided into the two main categories based on result type: qualitative, which only considers the contrast of objects, or quantitative, which aims to find exact values of the parameters of objects. For the qualitative types, non-iterative solution techniques are generally more desirable as there is a need only for the contrast value of the objects, therefore linearization techniques are generally applied in this type which typically works faster than iterative ones. On the other hand, quantitative methods generally use iterative methods to converge real values. In the final stage, all the solution methods are restricted by limited real-world conditions such as limited aperture, band-limited data, single-view restriction noisy environments, etc.

Qualitative imaging methods find the contrast of object parameters instead of exact value need less prior knowledge and generally one-shot results. This is the reason why these methods are advantageous in application over the quantitative and non-linear solution methods. There are several common methods such as Factorization Method (FM) [14] and Sampling Methods (Linear SM [LSM] [15], Direct SM [16], Orthogonal SM [17], etc.). These methods generally use limited aperture sampled data over a transfer plane (generally spherical plane) and solve linearized forward equations by using regularization or eigenvalue decomposition techniques such as Tikhonov regularization, and truncated singular value decomposition (TSVD) [18]. Differently from these techniques, several methods use near-field data with better reconstruction such as Near Orthogonal Sampling Method (NOSM) [19].

There are many methods in the literature that solve nonlinear equations and give quantitative results. These methods highly depend on the domain function (which is called the Green function) and object information (boundary conditions are sound-soft or not). Once the system is defined as required for a particular problem, the nonlinear equation could be solved iteratively as in Newton-type methods, Contrast Source Inversion (CSI), etc. In the fundamental Newton-Kantorovitch method, the non-linear equation is first linearized and solved by using the forward equation with regularization techniques [20, 21]. But this approach is computationally extensive and inefficient, because of that new methods such as CSI, which uses the cost function of non-linear equation [22] to reach the closest value, or one of the recently purposed modified type Newton method, which uses linearization in both object and data equation to enhance convergence rates [23].

Deconvolutional models are also another technique that use the transfer function of the imaging domain at the expense of making extensive calibration procedures but at the same time gives quantitative results [24]. Holographic imaging is one of the recently emerged deconvolutional method that gives quantitative and faster results [38]. Unlike other common quantitative methods, it provides one-shot results and does not need any prior knowledge of the object boundary or domain itself. However, it requires a better calibration procedure, a better choice of reference objects, and sufficient spatial data. Holography is applied to the microwave field in many areas such as antenna pattern determination [25], security imaging [26], tomography in medical imaging, non-destructive inspection or dielectric measurement on materials [27–29] holographic quantitative imaging as similarly in this thesis.

One mostly seen and possible common problem in microwave holographic imaging and other measurement systems that use antenna is measuring and calibrating of antenna. Measuring s-parameters for near or far-field data in larger apertures requires a longer and more stable calibration procedure. Due to stability requirement of system, enable any way that reduce sampling in calibration would enhance the calibration quality. Simulation based modeling is one of the approach to reduce sampling in measurement for reference object calibrations. One way of modeling the antenna is spherical wave expansion which is a general method used for expanding fields into the dipole modes, and antenna characterization for scattering analysis in both near-field and far-field modes [30, 31].

In the near-field characterization of spherical near-field measurements, using all space points on the spherical surface circumference AUT and using dense sampling in the frequency band for expansion would be difficult, particularly impossible in real-world experiments [32]. Therefore techniques such as compressed sensing (CS) based on optimization of sampling matrix that reduce sample in space by considering mutual coherence [33] is used. For reduced frequency samples, especially for wideband antennas, techniques like the Singularity Expansion Method, namely the Cauchy Method are applied to spherical expansion coefficients [34]. Also, the far-field of an antenna can be obtained by applying the near-to-far-field transformation, the way through spherical wave expansions. This could be done by many ways such as non-planar or planar sampling or using efficient algorithms like multi-level domain decomposition [35, 36]. Also even this sampling operation could applied with aid of the UAV for only far-field sampling [37].

2. QUANTITIVE MICROWAVE HOLOGRAPHIC IMAGING

2.1 Microwave Imaging

The microwave imaging reconstruction aims to find the electrical parameters of the unknown scatterers by considering the problem in the form of an inverse scattering equation. The inverse scattering solution basically aim to obtain the relative permittivity contrast ($\Delta\varepsilon_r = \varepsilon_r - \varepsilon_{r,b}$) or permeability, conductivity of the scatterer material, which is the difference value of relative permittivity of a scatterer (ε_r) and the background ($\varepsilon_{r,b}$). This problem is defined using the integral equation of forward scattering in (2.1) which uses the total field ($E^{tot}(r', r_j; \omega)$) in that area, the green function ($G(r, r')$) of scene.

$$E^{tot}(r_j;\omega) = E^{inc}(r_i;\omega) + k_b^2 \int_{\Omega} \Delta\varepsilon_r \underline{\mathbf{G}}(r_i, r';\omega) E^{tot}(r', r_j;\omega)\, d\Omega \tag{2.1}$$

There are many theorem is exist in literature to find contrast but it is hard to find both give result as quantitative and has lower computationally complex enough. The various conventional linearization methods gives possibly qualitative result but also there are some proposed linear methods are exist that provide quantitative results uses regularization in (2.1). In these methods forward equation solved many times to converge actual values with using the cost function that difference of E^{tot} and scattererr integral itself. Although, iterative methods are intuitive and the first to come to mind for solving equations, they are computationally expensive and it's solutions could not be converge.

Linearization is another approach for solving the equation as qualitative and also for quantitative methods like that used in this work. It can be applied by using Born and Rytov or both combinations of these types. As non-linearity in the forward equation occurs due to internal scattering fields, which also result from the equation itself, in the integral kernel. These methods handle these internal fields ($E^{internal}$) under the small internal scattering or the constant phase variation assumptions to remove the non-linearity part. Hence, the internal scattering directly depends on the scatterer and so the scatterer directly affects the quantitative result precision. If the scattering particles in the object are too reflective, the result may deviate from the true values, and therefore linearization is generally preferred in qualitative approaches.

$$E^{sca}(r_j;\omega) = k_b^2 \int_{\Omega} \Delta\varepsilon_r \underline{\mathbf{G}}(r_i, r'; \omega) E^{internal}(r', r_j; \omega)\, d\Omega \tag{2.2}$$

The linearization scattered field equation given in (2.2), can computed in both time and spectral domain. In this thesis, only spectral reconstruction is concerned as it is intended to resolve convolutional field integral. Due to spectral reconstruction, the convolutional kernel could have handle as system transfer function which will called as Point Spread Function (PSF) and this function will be directly linked our system with contrast object function. Spectral reconstruction and linearization will also help us transform our scattering equation into a linear system that is easily usable in devices.

2.2 Linearization

Since the approaching directly or iteratively to the forward equation that is given (2.1) in nonlinear form, is exhaustive, linearization methods have become attractive ways to solve equations faster and feasible. Linearization methods are used so that the environment has negligible multiple scattering and mutual coupling. This approach gives a solution that uses a function independent from the solution within the kernel while compromising the exact forward solution. There are two main approaches for linearization, one uses a small internal scattering assumption based on Born approximation, and the other is the small refractive deviation assumption based on Rytov approximation. In Born approximation total E-field in the object domain is taken as the incident E-field due to the neglected small scattering field beside the large incident field ($E^{tot}(r') \approx E^{inc}(r')$). It corresponds to decomposing the object domain into discrete, independent dipole particles. To apply the Born approximation, the contrast and size of the object have to be limited under the related equation (2.3), which takes the contrast function and uses the minimum circumference in the angle metric of the scatterer.

$$k_b a \|\chi(\mathbf{r})\| < 2\pi\gamma, \tag{2.3}$$

where k_b is background wave-number, a is smallest sphere circumscribe the scatterer object, and γ is a constant number which is defined as differently in the literature, generally is 0.25. $\chi(r) = \frac{\mu_r \varepsilon_r - \mu_b \varepsilon_b}{\mu_b \varepsilon_b}$ is normalized contrast function defined with relative complex permittivity (ε_ζ) and permeability (μ_ζ) for both background ($\zeta = b$) and scatterer ($\zeta = s$). In this condition most effective part is a high-frequency limitation of approximation due the maximum limiting scenario.

In Rytov approximation, an object that has a large scale compared to the wavelength is considered and focused on the phase deviations within a small contrast environment and written in phase summation ($E^{tot}(r) = E^{inc}(r) exp[\sum_{i=0}^{n} \psi_i(r)]$). In the first-order Rytov approximation, the total field written in (2.4) that only uses first order of phase summation term (where zero term corresponds to background or incident field namely) and so uses directly scattered field in equation in place of the total field. It can be clearly seen there is a phase wrapping problem occurs in Rytov approximation when expand equation in phasor form (2.5).

$$E^{tot}(r) = E^{inc}(r) exp[E^{sc}(r)/E^{inc}(r)] \tag{2.4}$$

$$E^{sc}(r) = E^{inc}(r). \left(ln \frac{|E^{tot}|}{|E^{inc}|} + i[\phi_{tot} - \phi_{inc}] \right) \tag{2.5}$$

There is also a limitation for Rytov approximation depends only contrast term that occurs due to neglected remaining phases other than first one (2.6) [38].

$$|(k(r') - k_b)/k_b| \ll 1 \tag{2.6}$$

These conditions can be seen as a very strict limitation due to their impractical in a real environment. Therefore, a variety of iterative methods, which use non-linear equations directly, has been suggested such as the Born iterative method, distorted Born iterative method, etc. As these methods are computationally extensive, there is a computational cost and accuracy trade-off between these methods and the linearization methods.

2.2.1 Combined born/rytov technique

Born approximation gives more accurate results in small scatterer that has high contrast while Rytov gives better results in small refractive variation and high-loss situations. Although, the Rytov approximation useful when we imaging wide and low contrast object, there is phase wrapping occurs with spatial position changes and applying unwrapping may not be works every time. So improved version is suggested which uses only real part of scattering equation in [39]. Taking to real parts of scattering equation leads to cross correlation of contrast and PSF function and resulted combined linear transform matrix consist of 3 rows of real and imaginary part of PSF's as in (2.7). In this approach, just only the real part of Rytov which is intentionally used for the prevent phase wrapping, and all parts in Born approximation are combined in the linear system and are solved with one of the ill-conditioned solvers like least-square, etc [40].

$$A_{combined} = \begin{bmatrix} \mathscr{F}_{2D}\{Re(A^{Born})\} & -\mathscr{F}_{2D}\{Im(A^{Born})\} \\ \mathscr{F}_{2D}\{Re(A^{Born})\} & \mathscr{F}_{2D}\{Im(A^{Born})\} \\ \mathscr{F}_{2D}\{Re(A^{Born})\} & -\mathscr{F}_{2D}\{Im(A^{Born})\} \end{bmatrix} \tag{2.7}$$

2.3 Spectral Holographic Reconstruction

2.3.1 Holographic imaging

Holographic imaging is one of the reconstruction approaches that we used in the linear inversion technique in the imaging problem. This technique is based on optical holography and it was first invented by Gabor in 1950's to improve electron microscopes [41]. The holography method is based on looking at the phase information beside the amplitude of the received signal to obtain the 3D intensity of the target. The phase information is gathered by superposition of background-wave with scattering wave as in interferometry, so the final received signal is complex data as a combination of amplitude and phase-shift information of the scattering object.

In electromagnetic scattering, the wave passing through an object changes how both phase and amplitude are compared to waves taking the same distance at the same angle in the free space. So, in the same manner, as in interferometric optical holography, microwave imaging uses the baseline measurements called reference object (RO) and the (OUT) measurements. In order to obtain interferometric phase and amplitude response of data, it subtracts RO measurements (S_{RO}) from OUT measurements (S_{OUT}) as in formulated in (2.8). Baseline measurements correspond to system response when there is no object in the scene and it contains background information.

$$S_{SP}(r_{tx}, r_{rx}, \omega; r_0') = S_{CO}(r_{tx}, r_{rx}, \omega; r_0') - S_{RO}(r_{tx}, r_{rx}, \omega) \tag{2.8}$$

2.3.2 Spectral reconstruction

Transforming the final scattering equation in the spectral transverse domain utilizes the decomposed domain into scattering modes and gives a way to solve the integral equation simply linearly instead of directly using 2D convolution. To enable the spectral decomposition of convolution, first, we have to determine the kernel of the integral equation. Under the Born approximation, our scattering equation (2.1) can be written in (2.9).

$$E^{sc}(r_{Tx}, r_{Rx}; \omega) = k_b^2 \iiint_{\Omega} \chi(r') \underline{\mathbf{G}}(r_{Rx}, r'; \omega) E^{inc}(r', r_{Tx}; \omega)\, dr' \tag{2.9}$$

Let's take the resolvent kernel as the dot product term in the integral that depends on the ξ'th transmitter and receiver pair and write it as the object-centered form in (2.10). It should be noted that Tx and Rx only change in x-y plane for the sake of simplicity, and so the resolvent kernel only scans over x-y. It is worth to mentioning that the Green function could be modeled with the total field of the receiver antenna in the same space coordinates when there is the object exists.

$$K_{\xi}(x-x', y-y', z'; \omega) = \underline{\mathbf{G}}_{Rx_{\xi}}(x, y, z; x', y', z'; \omega) E^{inc}_{Tx,\xi}(x, y, z; x', y', z'; \omega) \tag{2.10}$$

Final convolution is written in the form in (2.11), where scattering fields directly equal to 2D convolution of $f(x,y,z) = k_0 \chi(x,y,z)$. There is only $r_{\xi} = (x,y)$ dependence on the scattering field as pairs being in constant z_{ξ} slices.

$$E^{sc}_{\xi}(x, y; \omega) = \int_{z'} \int_{y'} \int_{x'} f(x', y', z') K_{\xi}(x-x', y-y'; z'; \omega)\, dx'\, dy'\, dz' \tag{2.11}$$

If we take 2D Fouirer transform (FT) respect to transverse axis (x, y) of the (2.11), the equation becomes the multiplication of spectral terms (2D Fourier of f and K_{ξ}) under a single integral sum over layers and the problem of ill-posedness has become dependent on one dimension only.

$$\widetilde{E}^{sc}_{\xi}(k_x, k_y; \omega) = \int_{z'} \widetilde{F}(k_x, k_y, z') \widetilde{K}_{\xi}(k_x, k_y, z'; \omega)\, dz' \tag{2.12}$$

where $\widetilde{F}(k_x, k_y, z') = \mathscr{F}_{2D}\{\chi(x', y', z')\}$ is the spectral contrast function, and if we discretize the z domain, we have to transform our integral equation into the discrete summation. In order to do that Δz multiplier is added into the equation in place of the

dz'. Finally, we will get summation over layers of spectral product as in (2.13) for each discrete frequency.

$$\widetilde{E}^{sc}_{\xi}(k_x,k_y;\omega) = \sum_{n=1}^{N_z} \widetilde{F}(k_x,k_y,z'_n)\widetilde{K}_{\xi}(k_x,k_y,z'_n;\omega)\Delta z' \tag{2.13}$$

This equation indicates a linear system of equations with low rank, therefore it is necessary to use inverse methods and/or regularization to obtain a quantitative or qualitative solution. In the practical experiments, the scattering electric field could not measured directly. Therefore it is necessary to transform our electric field equality into the equation that uses measurable quantities. For such a problem, Vector Green Integral (VIE), which is explained in detail in the later chapters, replaces the Green function of the system with the total electrical field with respect to the receiver, into the scattering parameter equation (2.14). It is important to note that the total field in this equation is measured as if both antennas exist in the scene.

$$S^{sc}_{\xi}(\omega) = \int_{\Omega} f(x',y',z')E^{inc}_{Tx,\xi}(x',y',z';\omega)E^{tot}_{Rx,\xi}(x',y',z';\omega)d\Omega \tag{2.14}$$

Hence, our new convolution kernel is equal to (2.15),

$$K_{\xi}(r';\omega) = E^{inc}_{Tx,\xi}(r';\omega)E^{tot}_{Rx,\xi}(r';\omega) \tag{2.15}$$

And therefore, the (2.16) is will be finalized as below,

$$\widetilde{S}^{sc}_{\xi}(k_x,k_y;\omega) = \sum_{n=1}^{N_z} \widetilde{F}(k_x,k_y,z'_n)\widetilde{K}_{\xi}(k_x,k_y,z'_n;\omega) \tag{2.16}$$

The final equation could be written as a linear system of equations for each k-space position $\boldsymbol{k} = (k_x,k_y)$,

$$B(\boldsymbol{k}) = A(\boldsymbol{k})f(\boldsymbol{k}) \tag{2.17}$$

And for each transmitter-receiver pair (ξ) linear system parts can be written as,

$$B(\boldsymbol{k}) = \begin{bmatrix} B_1(\boldsymbol{k}) & \dots & B_{N_T}(\boldsymbol{k}) \end{bmatrix}^T_{N_T N_\omega x 1} \tag{2.18}$$

$$A(\boldsymbol{k}) = \begin{bmatrix} A_1(\boldsymbol{k}) & \dots & A_{N_T}(\boldsymbol{k}) \end{bmatrix}^T_{N_T N_\omega x N_z} \tag{2.19}$$

$$f(\boldsymbol{k}) = \begin{bmatrix} \widetilde{F}(\boldsymbol{k},\bar{z}_1) & \dots & \widetilde{F}(\boldsymbol{k},\bar{z}_{N_z}) \end{bmatrix}^T_{N_z x 1} \tag{2.20}$$

where,

$$B_{\xi}(\boldsymbol{k}) = \left[\widetilde{S}^{sc}_{\xi}(\boldsymbol{k},\omega_1) \quad \dots \quad \widetilde{S}^{sc}_{\xi}(\boldsymbol{k},\omega_{N_\omega})\right]^T, \xi = 1,\dots,N_T \tag{2.21}$$

$$A_{\xi}(\boldsymbol{k}) = \begin{bmatrix} \widetilde{K}_{\xi}(\boldsymbol{k},\omega_1;\bar{z}_1) & \dots & \widetilde{K}_{\xi}(\boldsymbol{k},\omega_1;\bar{z}_{N_z}) \\ \vdots & \ddots & \vdots \\ \widetilde{K}_{\xi}(\boldsymbol{k},\omega_{N_\omega};\bar{z}_1) & \dots & \widetilde{K}_{\xi}(\boldsymbol{k},\omega_{N_\omega};\bar{z}_{N_z}) \end{bmatrix} \tag{2.22}$$

These equation systems will be well-conditioned if there are enough z layers for corresponding frequency and Tx-Rx data points. As condition

2.3.3 Point spread function (PSF)

One way to resolve the kernel in (2.11) is by using a point scatterer (PS) for each position in the imaging domain and thus obtaining the system response of the domain. This method corresponds to the extracting transfer function of the domain itself in the assumption of linearity of the system (due to the Born approximation), hence the resolving kernel of the point scatterer is an actually kernel of Dirac convolution. This point scatterer object is also called a calibration object (CO) and in order to satisfy the linearity assumption mentioned above, it has to satisfy Born approximation conditions and resolution requirements, which are examined in detail in later sections. Then, the contrast function of the PS will be equal to the constant contrast value (2.23) due to the small contrast change in such a small area.

$$f(x,y,z) = \Delta\varepsilon_{CO}\delta(x,y,z-z_i) \tag{2.23}$$

If we write the scattering convolution for the PS in (2.10) using (2.23), the CO kernel will go outside the equation directly for such small Dirac-like scatterer for each i'th position in the domain as written in (2.24). It important to notice that in this PSF formula, there is a normalization constant from CO itself and normalization values depends on PS volume and its contrast.

$$S^{sc}_{\xi}(x_i,y_i;\omega) \approx k_b^2 K_{\xi}(x_i,y_i;\hat{z};\omega)\Delta\varepsilon_{CO}\Omega_{CO} \tag{2.24}$$

Therefore the PSF kernel can be written as finally,

$$K_{\xi}(x_i,y_i;\hat{z};\omega) \approx \frac{S^{sc}_{\xi}(x_i,y_i;\omega)}{\Delta\varepsilon_{CO}\Omega_{CO}} \tag{2.25}$$

2.3.4 Fundamental resolution and sampling limits for imaging

Limitations of spatial resolution are determined by the ability to resolve two scatterers from each other and depend physically on the discrimination of two consecutive wave peaks scattered from objects. While range resolution (2.26) depends on the bandwidth (B) inversely as in radar theory, cross-range resolution (2.27) depends on both maximum wavelength (λ) and acquisition aperture (α_{max}).

$$\delta_z = \frac{c}{2B}, \tag{2.26}$$

$$\delta_{x,y} = \frac{\lambda_{min}}{4 sin \alpha_{max}}, \tag{2.27}$$

Although cross-range fields could change with antenna pattern and antenna setup in measurement if pattern width is wide enough to illuminate acquisition aperture in far-field or antenna works in the near-field, the cross-range resolution does not depend on the antenna pattern itself [42]. But as in the real measurements, bandwidth becomes the main problem for the range resolution, omnidirectional antennas as dipole or resonator types antennas are not as feasible as horn-like antennas with directional patterns and wideband matching. A horn antenna was chosen for scanning to meet simultaneously bandwidth and beam-width requirements. Also, it is the reason why the low-directional antennas are mostly preferred in imaging applications [43].

Frequency sampling rates are determined by maximum range (R_{max}) from a similar equation given in (2.26). R_{max} could be determined by the aperture size between the outermost antenna if two antenna and transmission coefficients are used for imaging. This number can be calculated by wave number and phase shift limit where phase wrapping or π angle occurs (2.28).

$$2R_{max}\Delta k < \pi, \qquad \Delta f < \frac{c}{4R_{max}} \tag{2.28}$$

Or alternatively, this inequality can be given by frequency sample defined with bandwidth (2.29) as in [44],

$$N_f > \frac{2R_{max}}{c/2BW} \tag{2.29}$$

2.3.5 Range domain solution

The spectral reconstruction decomposes cross-range convolution into independent point equations, and there will be only a linear system related to the range-to-frequency transform. As depicted in the sections above, as range or sample points increases in system condition can be increase but this increment restricted by range resolution condition (2.29). This condition depends on range resolution in the system as range space is sliced according to resolution limits written in (2.26). But as there can be noise in the measured OUT data and the equation system could be badly scaled and condition number is high. Also, hence the equation system is initially over-determined, least square type solution methods has to be used for obtain result. In the solution regular iterative LSQR or directly QR decomposition methods applied. Typical values are defined as for N_z is between 3 and 20 in [48].

3. ANTENNA SYSTEM MODELLING AND OBTAINING CALIBRATION DATA

3.1 Antenna Modeling In Near And Farfield Regions

The antenna directivity affects the imaging resolution and quality of the image directly, as well as affects the noise accepted from other antenna reception angles. In imaging applications, directive and wideband antennas, such as horn and Vivaldi antennas, are preferred to enhance the quality of both range and cross-range resolutions due to the reasons mentioned in previous sections. A highly directive antennas have a wider aperture area, and therefore it has a wider near-field range compared to a small-sized antenna due to its aperture size according to the far-field region formula ($FF = 2D^2/\lambda$). In near-field imaging applications, this range becomes important, especially for highly directive antennas, as antennas in such close spaces fall into the near-field working region.

As our proposed method uses the simulated antenna model in the near-field region for the simulated calibration procedure, some way to find it is required for an identical numerical model that transforms the antenna currents into the S-parameter measurements. This transform can be done efficiently by using the VIE of the modeled antenna's fields with the Spherical Wave Expansion for the antenna currents [31]. This method can be seen as another look for the addition theorems in electromagnetic theory and it is related and can be usable with mode matching techniques [45].

The key idea here is the expansion of antenna e-fields into their spherical harmonic functions and write the dyadic transfer function in VIE as a these fields' expansion. This derivation is done by equating these antenna harmonics with each harmonic from the object domain on the reference plane by using the reciprocity relation of the antenna and using the complete orthogonality sets of harmonics as in the mode-matching technique. E-field on the reference plane can be expressed by multi-pole expansion as in (3.1) for the divergence-free fields [46].

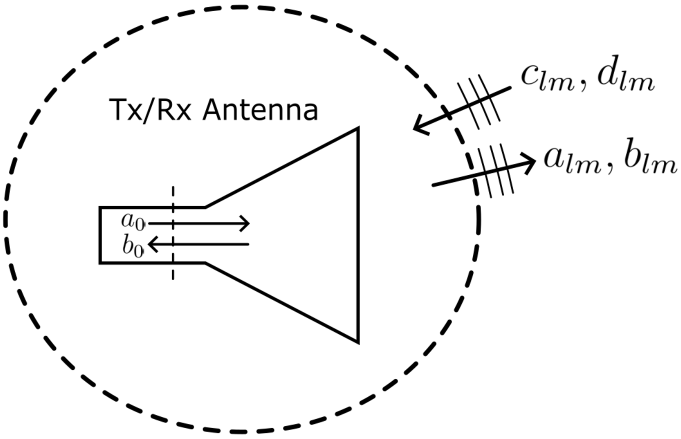

Figure 3.1 : Multipole Expansion Representation On the Antenna Reference Plane.

$$E(r) = \sum_{lm}[a_{lm}M_{lm}(r) + b_{lm}N_{lm}(r) + c_{lm}\Re M_{lm}(r) + d_{lm}\Re N_{lm}(r)] \tag{3.1}$$

$$M_{lm}(\boldsymbol{r}) = \nabla x[\boldsymbol{r}\psi_{lm}(\boldsymbol{r})],\ N_{lm}(\boldsymbol{r}) = \frac{1}{k}\nabla x M_{lm}(\boldsymbol{r}), \tag{3.2}$$

$$\psi_{lm}(r) = Y_{lm}(\theta,\phi)z_l(kr) \tag{3.3}$$

where m and l are pole coefficients that represent variations and directions of poles, M_{lm} and N_{lm} are vector wave functions defined in (3.2), a_{lm} and b_{lm} are expansion coefficients for outgoing waves while c_{lm} and d_{lm} are incoming waves coefficients. Vector wave functions are derived by vector equation defined in (3.3). Where Y_{lm} is the spherical wave function and $z_l(kr)$ is one of the spherical Bessel or Hankel functions.

Refer to the detailed derivation from [47], the below derivations express antenna voltages as a scattering equation. The antenna input voltage, which is our final function for the derivation, can be written as (3.4) and the incident field can be written as (3.6) using (3.5) and (3.1) for only incident waves. Here small e_{inc} is the normalized incident field with transmission or calibration coefficient a_0 which will be our final goal for the calibration procedure.

$$b_0 = \sum_{lm}(u_{c;lm}c_{lm} + u_{d;lm}d_{lm}) \tag{3.4}$$

$$a_{lm} = a_0 t_{a;lm},\ b_{lm} = b_0 t_{b;lm} \tag{3.5}$$

$$E^{inc}(r) = a_0\sum_{lm}[t_{a;lm}M_{lm}(r) + t_{b;lm}N_{lm}] = a_0 e^{inc}(r) \tag{3.6}$$

Then, by using the green function equation from (3.7) and our general scattered field equation (2.1), the scattering field can be written for expansion as in (3.8).

$$\underline{\mathbf{G}}(r,r') = ik\sum_{lm}\frac{1}{l(l+1)}[\Re M_{lm}(r)\hat{M}_{lm}(r') + \Re N_{lm}\hat{N}_{lm}(r')] \tag{3.7}$$

$$E^{scat}(r) = \int_{\Omega'} \left(ik \sum_{lm} \frac{1}{l(l+1)} \left[\Re M_{lm}(r) \hat{M}_{lm}(r') + \Re N_{lm} \hat{N}_{lm}(r') \right] \right) . \chi(r') E^{tot}(r') d\Omega' \tag{3.8}$$

And, changing integral with summation, the equation will be as in (3.9)

$$E^{scat}(r) = \sum_{lm} c_{lm} \Re M_{lm}(r) + d_{lm} \Re N_{lm}(r) \tag{3.9}$$

And finally, if we substitute c_{lm} and d_{lm} from (3.9) into the (3.4), the equation becomes in (3.10),

$$\begin{aligned} b_0 &= \sum_{lm} \frac{ik}{l(l+1)} \left[u_{c;lm} \int_{\Omega'} \hat{M}_{lm}(r') \chi(r') E^{tot}(r') d\Omega' + u_{d;lm} \int_{\Omega'} \hat{N}_{lm}(r') \chi(r') E^{tot}(r') d\Omega' \right] \\ &= \int_{\Omega'} \sum_{lm} \frac{ik}{l(l+1)} \left[u_{c;lm} \hat{M}_{lm}(r') + u_{d;lm} \hat{M}_{lm}(r') \right] \chi(r') E^{tot}(r') d\Omega' \end{aligned} \tag{3.10}$$

It can be clearly seen from the equation, the multiplier of the contrast function and total E-field function becomes our new green function called as the *Vector Green Function* and it can be written as in (3.11) for j'th receiver and total E-field from i'th transmitter. Also, it is important to notice that the vector green is independent of the receiver position (**r**) differently from dyadic Green.

$$b_0^j = \int g_j(r') \chi(r') E_i^{tot}(r') d\Omega' \tag{3.11}$$

Then, the S-parameter (3.12) is found for i'th transmitter to j'th receiver from the b_0^j equation by writing the normalized total field as in (3.6) and dividing both sides to a_0^j term.

$$S_{ji} = \int_{\Omega'} g_j(r') \chi(r') e_i(r') d\Omega' \tag{3.12}$$

3.1.1 An alternative form for the vector green function

Although the above derivation is useful, we still do not know the Vector Green function exactly. To obtain Vector Green, either would know the exact system model or more conveniently, use the incident fields to obtain system response using reciprocity relations $\left(\hat{M}_{l,-m}(r) = (-1)^m M_{lm}(r)\right)$ of an antenna in [31].

$$\begin{aligned} g(r) &= \frac{iZ_0}{2\omega\mu} \sum_{lm} (-1)^m . \left(t_{a;lm} \hat{M}_{l,-m}(r) + t_{b;lm} \hat{N}_{l,-m}(r) \right) \\ &= \frac{iZ_0}{2\omega\mu} \sum_{lm} \left(t_{a;lm} M_{lm}(r) + t_{b;lm} N_{lm}(r) \right) \end{aligned} \tag{3.13}$$

This equation (3.13) is known from (3.6) defined above, so Vector Green can be directly calculated by E-field (3.14).

$$g(r) = \frac{iZ_0}{2\omega\mu} e^{inc}(r) = -\frac{Z_0}{a_0 i\omega\mu} E^{inc}(r) \tag{3.14}$$

And, the S-parameter equation will be (3.15)

$$S_{ji} = \frac{iZ_0}{a_0^i a_0^j \omega\mu} \int_{\Omega'} E_j^{inc}(r').\chi(r').E_i^{tot}(r')d\Omega' \tag{3.15}$$

Here, based on the summation of the incident and total fields as well as the calibration coefficients (a_0^i for the transmitter and a_0^j for the receiver), which is our purpose in this thesis, we can directly find reflection and transmission coefficients. The calibration coefficients depend on the transmission line itself and do not change with the measurements in the ideal scenario. Hence, in our simulation-based calibration methodology, we only need single measurement data to calibrate our simulation-based results because there is a linear relation between calibration coefficients and scattering S-parameters. Also, these calibration coefficients can be found by direct measurements for real scenarios [47].

3.2 Obtaining Scattering Field Of The Calibration Object

As required PSF data is measured in each point of slice plane $\bar{z}$, the scattering field has to be computed over $x-y$ space. This operation corresponds to obtaining the transfer function of the domain or obtaining convolution data obtained with the point scatterer.

To obtain an identical scattering field of CO with a real measurement setup in simulation, there has to be an antenna with the same antenna characteristics but not an exact one. This is because the field distribution only depends on the antenna structure and the transmission line change phase and amplitude of the excited signal. Therefore, after a field identical to the real antenna is obtained, there is calibration with antenna coefficients as depicted in Section 3.1.

To obtain calibration data it is necessary that at least one sample data is taken from the real environment with the same CO object in order to calibrate the system's priorly known complex dielectric constant. After a single calibration point is obtained, the calibrated electrical field will be given the required S-parameter over the slant plane as the referring formula given in (3.15). If there is more than one antenna being used,

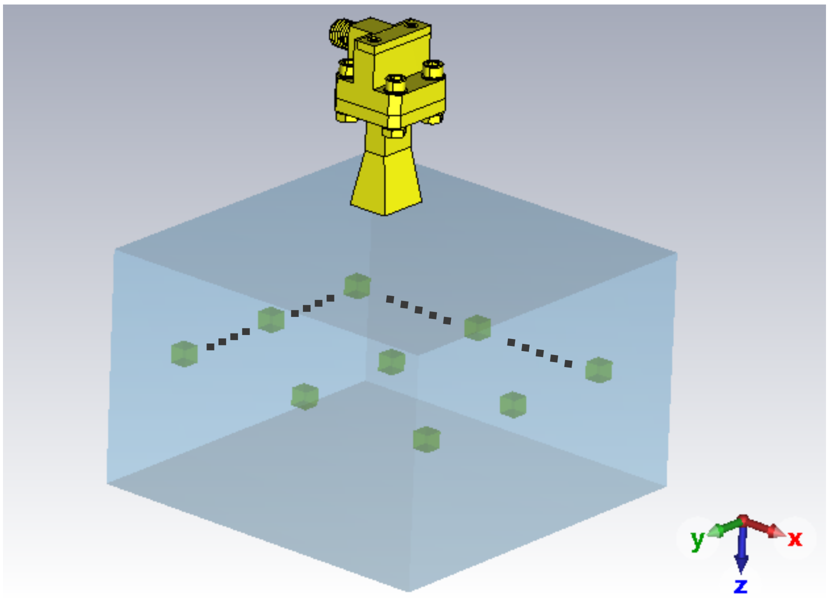

Figure 3.2 : Illustration of the calibration procedure corresponding to the actual measurement in scanning CO data.

two corresponding calibration coefficients are necessary to be known for each TX-RX pair. Also, it is important to notice that the total electrical field has to be obtained while other antennas and system parts are present.

This procedure could thought to be as scanning over a cartesian area on $[Vx, Vy]$ as in 3.2 and differently from real scanning, in this technique, directly small volume convolution operation could be applied over e-field data with corresponding epsilon of the CO object. Due to the convolutional process of such a small kernel, the scanning process would be accelerated. Before proceeding to our proposed calibration procedure and imaging operation, it is convenient to validate our PSF obtained from full-wave simulation with pre-used data from the [48]. The absolute value of PSF obtained in data of that research drawn left in the 3.3 and PSF obtained from full-wave simulation of scanning over each slant position drawn right in the same figure. For the comparison, identical CO (3mm x 2.6mm x 2mm, $\varepsilon_r = 7.85 + i3.01$) measurement is simulated on the full wave time domain simulation in CST Microwave Studio with identical horn antenna (A standard WR-28 waveguide-based horn antenna). As each of the $\bar{z}$ range has to be simulated separately for full space calibration in a direct full-wave solution, only the farthest one ($\bar{z} = 43.1mm$) is shown for comparison. From 3.3, two PSFs have since like data shape due to point scatterer, but there is corruption in measured one reason of constant noise on data during full one-axis measurement.

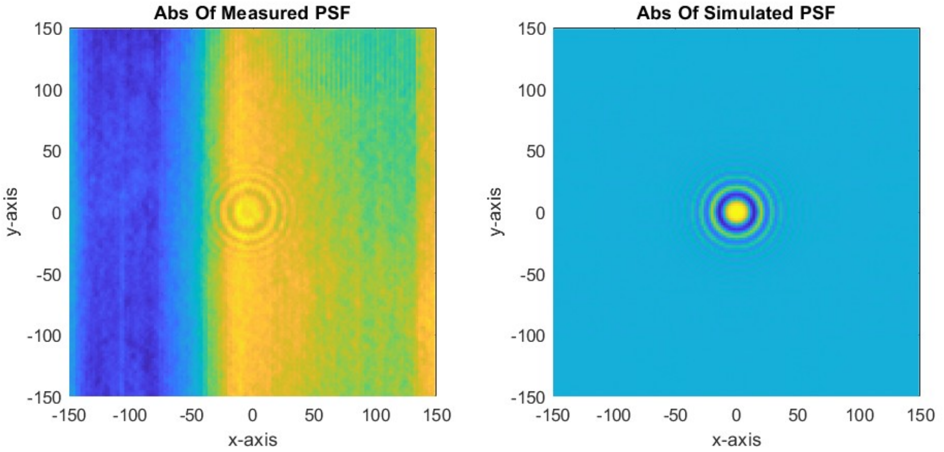

Figure 3.3 : Comparison of the absolute value of PSF from real measurement [42] with the PSF from simulation.

Therefore, we can conclude that the measurement PSF on simulation could block out the noise from setup-related changes.

3.2.1 Antenna calibration with simulation

Because of the exhaustive scanning operation of the direct scanning approach, it is not feasible to solve all spaces with a full-wave solver for QMH's calibration procedure. Therefore, we proposed using the VIE (3.15) with the obtained e-field instead of the direct solution. In this way, our processing time would equal the time that the convolution operation takes and the calibration procedure by simulation effort will be gradely reduced. To apply VIE, the antenna e-field is recorded in the imaging space similar to 3.2, and the total e-field is recorded using the CST Microwave Simulation tool where all other parts exist in a simulation.

4. IMAGING SETUP

The imaging setup for the QMH algorithm in this work is defined with only one antenna establishment for the sake of simplicity. In both setups, different objects and different CO values are tested.

4.1 Measurement Setup With Hertz Dipole Antenna

This measurement setup same as in [48] and consists of a hertz dipole (infinitesimal dipole) in the free-space environment. For this setup, we used the FEKO simulation environment to get more comparable results within the referenced and to show that the method is independent of the platform if adequate solver type and setup are provided. In this setup 1 to 13 GHz is used with 300 MHz steps and $240 \text{x} 240 mm^2$ imaging area calibrated with CO probe that is a 3 mm sized cube with complex permittivity value $\varepsilon_r = 1.8 - i0.15$. The imaging area is calibrated with 7.5 mm steps and there are 5 ranges considered which are 30, 50, 70, and 90 mm distances as in 4.1. At each slice, E-fields are obtained to get S11 data differently from the original work. For this reason, results differ from the real values.

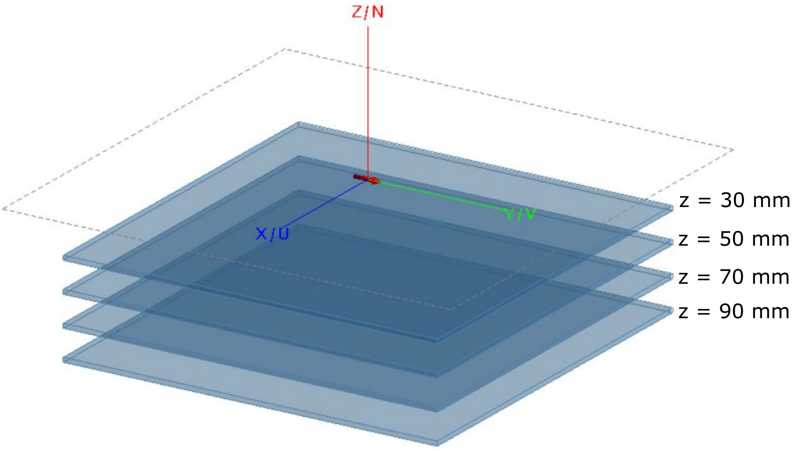

Figure 4.1 : Imaging setup with hertz antenna and corresponding imaging layers: z = 30,50,70,90.

4.1.1 PSF comparison with original work data

Firstly, we compare two PSF data as shown in figure 4.2: one is (S_{11}^{SIM}) from the original work which simulated with FEKO; the other is our obtained data (S_{11}^{VIE}) with the VIE algorithm. The error is calculated over each frequency point with (4.1) using total error from all space. According to the result, the overall error stays under %1 in total. The most error comes from edge points of the frequency band.

$$Error(\%) = 100 \cdot \frac{\sum_{x,y,z} \left(S_{11}^{VIE}(f) - S_{11}^{SIM}(f) \right)}{\sum_{x,y,z} S_{11}^{SIM}(f)} \tag{4.1}$$

Also, the range-based error obtained over on total frequency error in each layer can be seen in 4.3. According to this figure, most error comes from the farthest ranges as

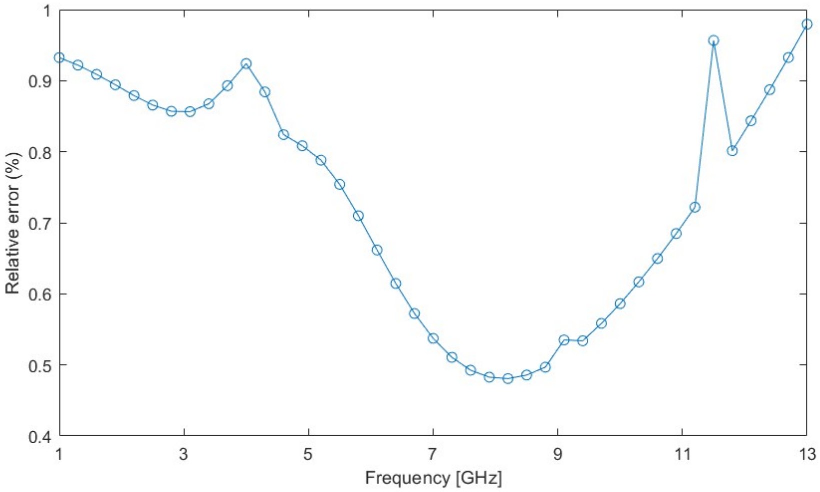

Figure 4.2 : Comparison of the PSF value over on total space error.

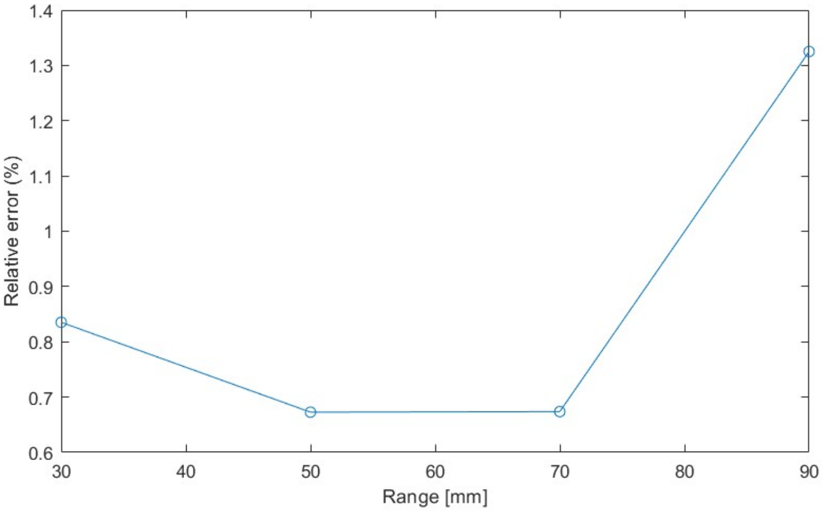

Figure 4.3 : Comparison of the PSF range error over on total frequency error.

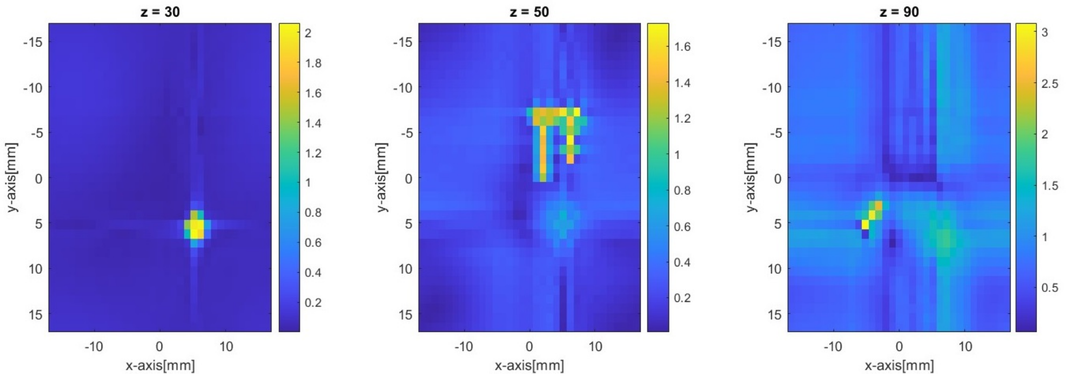

Figure 4.4 : Simulation results on multiple shapes.

over %1.3 of total error in full-wave simulation due to possible reason of increasing sampling error in e-field that obtained in simulation.

4.1.2 OUT result with VIE algorithm

The result of our algorithm on this setup can be seen in 4.4. This setup consists of three 4 layers with 3 shapes whose are; cylinder where ($\varepsilon_r = 1.8 - i0.12$) radius 11.25 mm with 3 mm height at the top, rectangular prism where ($\varepsilon_r = 2 - i0.2$) dimensions 15x30x3 mm^3 at the bottom and pi shape ($\varepsilon_r = 1.5 - i0.075$) at the mid-layer.

4.2 Measurement Setup With Half-Wave Dipole

This setup consists of a simple half-wave dipole antenna and a free-space environment as in work [49] and shown in 4.6. As we gather wideband data and work on a simulation environment, a corresponding half-wave dipole antenna is used for each frequency sample and placed above 15 mm from first layer. The frequency range is 4 to 16 GHz with 1 GHz steps and the area is 200x200x20mm^3. Calibration is done with 1 mm cube PS that has $\varepsilon_r = 1.1$ over the imaging area with 10 mm steps.

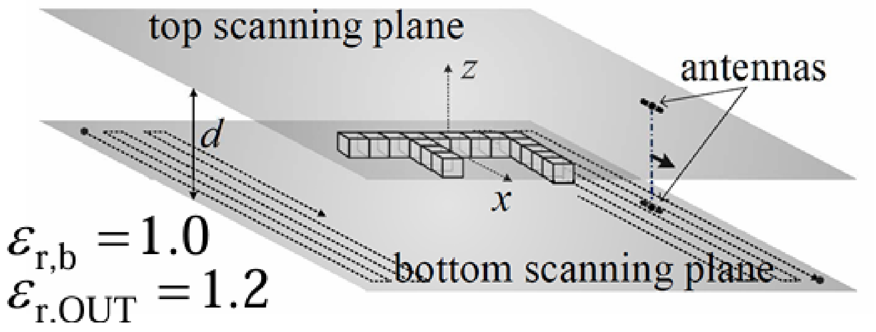

Figure 4.5 : F-shape simulation setup [49].

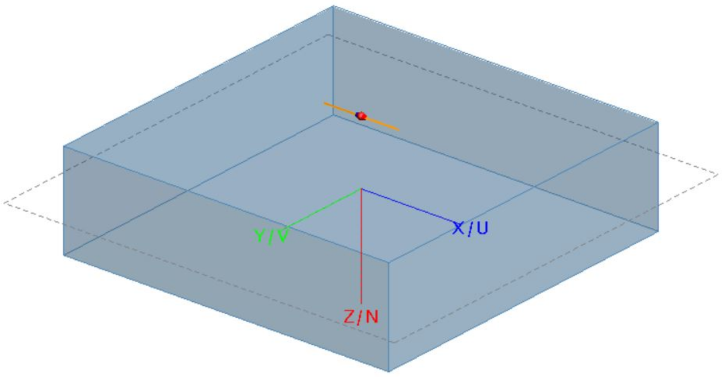

Figure 4.6 : Imaging setup with a dipole antenna and corresponding imaging domain.

According to the condition of Born approximation with circumference $a = \sqrt{2}$ and $\lambda_{max} = 18.8mm$, $\chi(r) < 3.3$ in (2.3) satisfied. Range resolutions are found from (2.26) and (2.27) as $\delta_z \approx 11.5mm$ and $\delta_{x,y} \approx 4.78mm$ and value given above adequately satisfy this conditions.

4.2.1 F-shape results

Simple F-shape simulated in this setup to validate our method with existing results given in [48]. There are 3 layers in the setup with only one object being imaging which is F-shape with permittivity $\varepsilon_r = 1.2$. The result can be seen in 4.7 and the F shape found at the 2nd layer with a 1.2 value. It is also important to note that the object's shadow is imaged in the previous domain, as shown in the figure. The

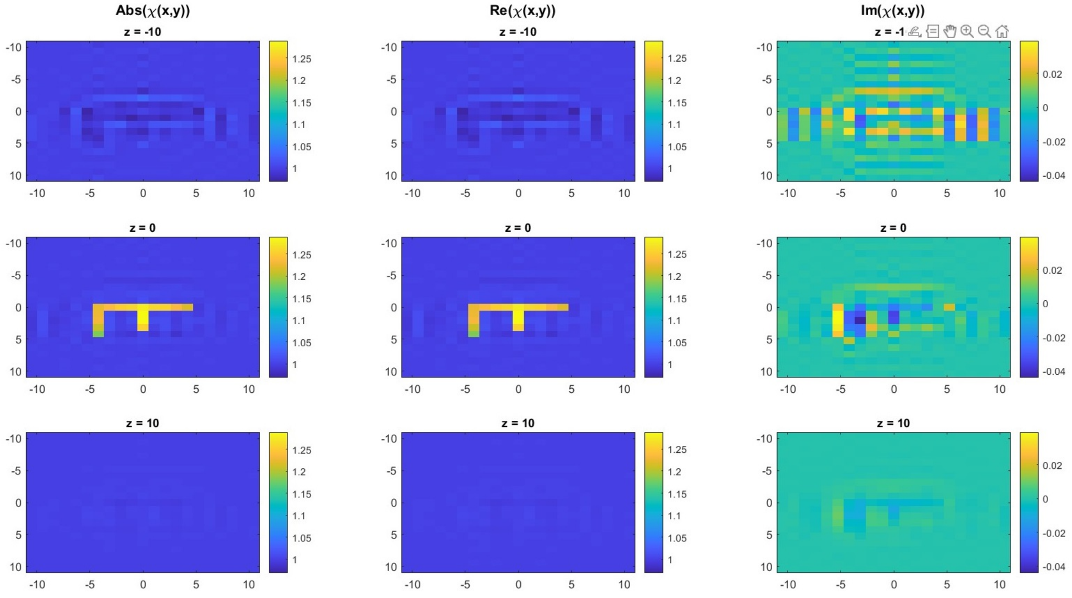

Figure 4.7 : F-shape imaging results (Left column: Absolute values , middle column: Real part, Right Column: Imaginary part).

F-shape's quantitative value being imaged is 1.2 in the $z = 0$ range slice. It can be seen from this result and compared with reference work, the VIE algorithm successfully provides the same PSF that resolves objects from OUT data.

5. CONCLUSION

In this thesis, a new calibration method for the quantitative microwave holography is proposed. The quantitative holograph requires a precise calibration for the imaging domain with the reference CO object. In the conventional method, this calibration procedure is conducted in overall space with a small scatterer object that has known dielectric permittivity. Our new calibration method eliminates this time-consuming and non-ideal calibration procedure by exchanging simulated calibration. Different from existing methods that use non-measurement data for calibration, such as range migration, our method uses an identical antenna setup and calibrates itself with real measurement values. In this way, calibration of both accelerated and real antenna patterns will be used for data gathering.

Calibration over simulation based on obtaining s-parameter data with the e-field obtained from the identical simulation of the real measurement setup. After the e-field is obtained, this data is connected to s-parameters with the VIE method. VIE method uses the Vector Green function inside the scattering equation kernel which can be also obtained from the incident e-field of the transmitter antenna. To simulate an identical setup, firstly the same antenna model with a real setup is constructed. As the holography method removes background effects from measurements, the simulation model only requires a one-point antenna calibration to match the exact transmission line characteristics with real transmitter and receiver parts. Overall, there is only one point of SP data, and background data called RO is used and PSF for each range is computed over a single SP data of antenna calibration. Also, with a known field each range with a desired starting point can chosen over the range domain.

For this work instead of using real measurements, simulation environments that use full-wave solvers such as CST and FEKO are used. Horn and different types of dipole antennas are tested for imaging setups, and existing works are validated with these simulation setups. Through these setups, different CO objects and test objects for imaging are used and results show objects are identified with similar precision and resulting error as in full-wave solvers. In conclusion, our method eliminates time-consuming and error-prone calibration procedures with a simulation-based approach. In addition, using the VIE further improves this method compared to the direct solver.

REFERENCES

[1] **Ning, J.**, **Han, F. and Zou, J.** (2024). A Direct Sampling Method and Its Integration with Deep Learning for Inverse Scattering Problems with Phaseless Data, *ArXiv*, *abs/2403.02584*, https://api.semanticscholar.org/CorpusID:268247845.

[2] **Hanabusa, T.**, **Morooka, T. and Kidera, S.** (2022). Deep-Learning-Based Calibration in Contrast Source Inversion Based Microwave Subsurface Imaging, *IEEE Geoscience and Remote Sensing Letters*, *19*, 1–5, doi: 10.1109/LGRS.2022.3169799.

[3] **Martin, B.**, **Edwards, K.**, **Jeffrey, I. and Gilmore, C.** (2023). Cycle-GAN-based Calibration of Microwave Imaging Systems, *2023 17th European Conference on Antennas and Propagation (EuCAP)*, pp.1–4.

[4] **Neira, L.M.**, **Van Veen, B.D. and Hagness, S.C.** (2017). High-resolution microwave breast imaging using a 3-D inverse scattering algorithm with a variable-strength spatial prior constraint, *IEEE Transactions on Antennas and Propagation*, *65*(11), 6002–6014.

[5] **Coşğun, S.**, **Bilgin, E. and Çayören, M.** (2020). Microwave Imaging of Breast Cancer with Factorization Method: SPIONs as Contrast Agent., *Medical physics*, https://api.semanticscholar.org/CorpusID:214616899.

[6] **Santos, K.C.**, **Fernandes, C.A.C. and Costa, J.R.** (2022). Feasibility of Bone Fracture Detection Using Microwave Imaging, *IEEE Open Journal of Antennas and Propagation*, *3*, 836–847, https://api.semanticscholar.org/CorpusID:251146452.

[7] **Scapaticci, R.**, **Tobon, J.**, **Bellizzi, G.**, **Vipiana, F. and Crocco, L.** (2018). Design and Numerical Characterization of a Low-Complexity Microwave Device for Brain Stroke Monitoring, *IEEE Transactions on Antennas and Propagation*, *66*(12), 7328–7338, doi: 10.1109/TAP.2018.2871266.

[8] **Ghavami, N.**, **Sotiriou, I.**, **Cano-Garcia, H. and Kosmas, P.** (2021). An experimental microwave imaging prototype for food quality assessment, *2021 XXXIVth General Assembly and Scientific Symposium of the International Union of Radio Science (URSI GASS)*, 1–3, https://api.semanticscholar.org/CorpusID:238993199.

[9] **Farina, L.**, **Scapaticci, R.**, **Vásquez, J.A.T.**, **Rivero, J.**, **Litman, A.**, **Crocco, L. and Vipiana, F.** (2019). Microwave Imaging Technology for In-line Food Contamination Monitoring, *2019 IEEE International Symposium on Antennas and Propagation and USNC-URSI Radio Science Meeting*, 817–818, https://api.semanticscholar.org/CorpusID:207829300.

[10] **Sheen, D.M.**, **McMakin, D.L. and Hall, T.E.** (2007). Near Field Imaging at Microwave and Millimeter Wave Frequencies, *2007 IEEE/MTT-S International Microwave Symposium*, pp.1693–1696.

[11] **Sheen, D.M.**, **Clark, R.T.**, **Tedeschi, J.**, **Jones, A.M. and Hall, T.E.** (2019). High-resolution 3D microwave imaging of a moving target using optical motion capture, ***D.A. Wikner and D.A. Robertson**, editors, Passive and Active Millimeter-Wave Imaging XXII*, volume10994, International Society for Optics and Photonics, SPIE, p.109940D, https://doi.org/10.1117/12.2519892.

[12] **Slaney, M.**, **Kak, A. and Larsen, L.** (1984). Limitations of Imaging with First-Order Diffraction Tomography, *IEEE Transactions on Microwave Theory and Techniques*, *32*(8), 860–874, doi: 10.1109/TMTT.1984.1132783.

[13] **Colton, D. and Kress, R.**, (2019). Inverse Electromagnetic Obstacle Scattering, Springer International Publishing, Cham, pp.273–302, https://doi.org/10.1007/978-3-030-30351-8_7.

[14] **Kirsch, A. and Grinberg, N.**, (2007). 1095 The factorization method for Maxwell's equations, The Factorization Method for Inverse Problems, Oxford University Press, https://doi.org/10.1093/acprof:oso/9780199213535.003.0005.

[15] **Cakoni, F.**, **Colton, D. and Monk, P.** (2011). *The Linear Sampling Method in Inverse Electromagnetic Scattering*, Society for Industrial and Applied Mathematics, https://epubs.siam.org/doi/abs/10.1137/1.9780898719406, https://epubs.siam.org/doi/pdf/10.1137/1.9780898719406.

[16] **Ito, K.**, **Jin, B. and Zou, J.** (2013). A direct sampling method for inverse electromagnetic medium scattering, *Inverse problems*, *29*(9), 095018.

[17] **Potthast, R.** (2010). A study on orthogonality sampling, *Inverse Problems*, *26*(7), 074015, https://dx.doi.org/10.1088/0266-5611/26/7/074015, doi: 10.1088/0266-5611/26/7/074015.

[18] **Tuo, X.**, **Zhang, Y.**, **Huang, Y. and Yang, J.** (2021). Fast Sparse-TSVD Super-Resolution Method of Real Aperture Radar Forward-Looking Imaging, *IEEE Transactions on Geoscience and Remote Sensing*, *59*(8), 6609–6620, doi: 10.1109/TGRS.2020.3027053.

[19] **Akıncı, M.N.**, **Çayören, M. and Akduman, I.** (2016). Near-Field Orthogonality Sampling Method for Microwave Imaging: Theory and Experimental Verification, *IEEE Transactions on Microwave Theory and Techniques*, *64*(8), 2489–2501, doi: 10.1109/TMTT.2016.2585488.

[20] **Roger, A.** (1981). Newton-Kantorovitch algorithm applied to an electromagnetic inverse problem, *IEEE Transactions on Antennas and Propagation*, *29*(2), 232–238, doi: 10.1109/TAP.1981.1142588.

[21] **Hohage, T. and Langer, S.** (2010). Acceleration techniques for regularized Newton methods applied to electromagnetic inverse medium scattering problems, *Inverse Problems*, *26*(7), 074011, `https://dx.doi.org/10.1088/0266-5611/26/7/074011`, doi: 10.1088/0266-5611/26/7/074011.

[22] **van den Berg, P.M.**, **van Broekhoven, A.L. and Abubakar, A.** (1999). Extended contrast source inversion, *Inverse Problems*, *15*(5), 1325, `https://dx.doi.org/10.1088/0266-5611/15/5/315`, doi: 10.1088/0266-5611/15/5/315.

[23] **Bilgin, E.**, **Doğu, S.**, **Coşğun, S. and Çayören, M.** (2020). A Modified Newton Method Formulation for Microwave Imaging, *2020 IEEE Asia-Pacific Microwave Conference (APMC)*, 1057–1059, `https://api.semanticscholar.org/CorpusID:231826410`.

[24] **Shumakov, D.S. and Nikolova, N.K.** (2018). Fast Quantitative Microwave Imaging With Scattered-Power Maps, *IEEE Transactions on Microwave Theory and Techniques*, *66*(1), 439–449, doi: 10.1109/TMTT.2017.2697383.

[25] **Smith, D.**, **Yurduseven, O.**, **Livingstone, B. and Schejbal, V.** (2014). Microwave imaging using indirect holographic techniques, *IEEE Antennas and Propagation Magazine*, *56*(1), 104–117, doi: 10.1109/MAP.2014.6821762.

[26] **Yurduseven, O.** (2014). Indirect microwave holographic imaging of concealed ordnance for airport security imaging systems, *Progress in Electromagnetics Research*, *146*, 7–13.

[27] **Ivashov, S.I.**, **Razevig, V.V.**, **Sergeev, D.L.**, **Bugaev, A.S.**, **Zhou, F.**, **Prokhanova, E.I.**, **Shcherbakova, A.V.**, **Dobrynin, S.N. and Vasilenkov, M.** (2022). An Example of Microwave Holography Investigation of an Old Orthodox Russian Icon Dated to 19th Century, *Heritage*, `https://api.semanticscholar.org/CorpusID:252413975`.

[28] **Ahmed, A.**, **Kumari, V. and Sheoran, G.** (2022). Non-Destructive Dielectric Measurement and Mapping Using Microwave holography, *2022 2nd Asian Conference on Innovation in Technology (ASIANCON)*, 1–4, `https://api.semanticscholar.org/CorpusID:252849478`.

[29] **Zhuravlev, A.V.**, **Razevig, V.V.**, **Ivashov, S.I.**, **Skrebkov, A. and Alekseev, V.** (2019). On the Use of Microwave Holography to Detect Surface Defects of Rails and Measure the Rail Profile, *Sensors (Basel, Switzerland)*, *19*, `https://api.semanticscholar.org/CorpusID:84842244`.

[30] **Marinović, T.**, **De Villiers, D.I.L.**, **Bekers, D.J.**, **Johansson, M.N.**, **Stjernman, A.**, **Maaskant, R. and Vandenbosch, G.A.E.** (2021). Fast Characterization of Mutually Coupled Array Antennas Using Isolated Antenna Far-Field Data, *IEEE Transactions on Antennas and Propagation*, *69*(1), 206–218, doi: 10.1109/TAP.2020.3016395.

[31] **Haynes, M. and Moghaddam, M.** (2011). Multipole and S-Parameter Antenna and Propagation Model, *IEEE Transactions on Antennas and Propagation*, *59*(1), 225–235, doi: 10.1109/TAP.2010.2090489.

[32] **Simonov, N. and Son, S.H.** (2021). Overcoming Insufficient Microwave Scattering Data in Microwave Tomographic Imaging, *IEEE Access*, *9*, 111231–111237, doi: 10.1109/ACCESS.2021.3103414.

[33] **Bangun, A. and Culotta-López, C.** (2022). Optimizing Sensing Matrices for Spherical Near-Field Antenna Measurements, *IEEE Transactions on Antennas and Propagation*, *71*, 1716–1724, `https://api.semanticscholar.org/CorpusID:249394640`.

[34] **Roussafi, A.**, **Fortino, N. and Dauvignac, J.Y.** (2016). Compact modeling of UWB antenna 3-D near-field radiation using spherical vector wave expansion and Cauchy methods, *IEEE Antennas and Wireless Propagation Letters*, *16*, 173–176.

[35] **RodriguezVarela, F.**, **SierraCastafier, M. and GalochaIragüen, B.** (2018). Multi-Level Spherical Wave Expansion for Fast Near-Field to Far-Field Transformation, *2018 AMTA 2018 Proceedings*, 1–6, `https://api.semanticscholar.org/CorpusID:57764045`.

[36] **Xu, C.**, **Gan, H.**, **Peng, H.**, **Jiang, C. and Xu, Q.** (2020). Far-field Modeling for Non-planar Array Based on Spherical Wave Expansion, *2020 International Conference on Microwave and Millimeter Wave Technology (ICMMT)*, 1–3, `https://api.semanticscholar.org/CorpusID:233136064`.

[37] **Gueuning, Q.**, **Craeye, C.**, **de Lera Acedo, E. and Brown, A.K.** (2023). Improving the accuracy of a model-based approach for the near-field measurement of antenna arrays with UAVs, *2023 17th European Conference on Antennas and Propagation (EuCAP)*, IEEE, pp.1–3.

[38] **Tajik, D.**, **Kazemivala, R. and Nikolova, N.K.** (2022). Real-Time Imaging With Simultaneous Use of Born and Rytov Approximations in Quantitative Microwave Holography, *IEEE Transactions on Microwave Theory and Techniques*, *70*(3), 1896–1909, doi: 10.1109/TMTT.2021.3131227.

[39] **Tajik, D., Nikolova, N.K. and Noseworthy, M.D.** (2019). Improving Quantitative Microwave Holography Through Simultaneous Use of the Born and Rytov Approximations, *2019 16th European Radar Conference (EuRAD)*, pp.281–284.

[40] **Kazemivala, R., Tajik, D. and Nikolova, N.K.** (2022). Simultaneous Use of the Born and Rytov Approximations in Real-Time Imaging With Fourier-Space Scattered Power Mapping, *IEEE Transactions on Microwave Theory and Techniques*, *70*(5), 2904–2920, doi: 10.1109/TMTT.2022.3157728.

[41] **Koechner, W., Balasubramanian, N., Gladden, J.W., Leighty, R.D., Kurtz, R.L., Liu, H.K. and Owen, R.B.** (1979). *Handbook of Optical Holography*, Elsevier, `http://dx.doi.org/10.1016/C2009-0-22049-6`.

[42] **Nikolova, N.K.** (2017). *Introduction to Microwave Imaging*, EuMA High Frequency Technologies Series, Cambridge University Press, Cambridge, `https://www.cambridge.org/core/books/introduction-to-microwave-imaging/45B0A0062CC0B86BBAF632A6B9DFE39F`.

[43] **Tsai, C.H., Chang, J., Ou Yang, L.Y. and Chen, S.Y.** (2018). 3-D Microwave Holographic Imaging With Probe and Phase Compensations, *IEEE Transactions on Antennas and Propagation*, *66*(1), 368–380, `https://ieeexplore.ieee.org/abstract/document/8093651`, conference Name: IEEE Transactions on Antennas and Propagation, doi: 10.1109/TAP.2017.2768567.

[44] **Sheen, D., McMakin, D. and Hall, T.** (2001). Three-dimensional millimeter-wave imaging for concealed weapon detection, *IEEE Transactions on Microwave Theory and Techniques*, *49*(9), 1581–1592, doi: 10.1109/22.942570.

[45] **Martin, P.A.** (2024). Another look at addition theorems for vector spherical wavefunctions, *Mathematical Methods in the Applied Sciences*, *47*(16), 12443–12459, `https://onlinelibrary.wiley.com/doi/abs/10.1002/mma.9987`, `https://onlinelibrary.wiley.com/doi/pdf/10.1002/mma.9987`, doi: https://doi.org/10.1002/mma.9987.

[46] **Chew, W.C.**, (1995). Dyadic Green's Functions, Waves and Fields in Inhomogenous Media, IEEE, pp.375–428, `https://ieeexplore.ieee.org/document/5271020`, conference Name: Waves and Fields in Inhomogenous Media.

[47] **Haynes, M. and Moghaddam, M.** (2011). Vector Green'S function for S-parameter measurements of the electromagnetic volume integral equation, *2011 IEEE International Symposium on Antennas and Propagation (APSURSI)*, pp.1100–1103.

[48] **Doğu, S.**, **Tajik, D.**, **Akıncı, M.N. and Nikolova, N.K.** (2023). Improving the Accuracy of Range Migration in 3-D Near-Field Microwave Imaging, *IEEE Transactions on Microwave Theory and Techniques*, *71*(8), 3540–3551, doi: 10.1109/TMTT.2023.3242322.

[49] **Tu, S.**, **McCombe, J.J.**, **Shumakov, D.S. and Nikolova, N.K.** (2015). Fast quantitative microwave imaging with resolvent kernel extracted from measurements, *Inverse Problems*, *31*(4), 045007, `https://dx.doi.org/10.1088/0266-5611/31/4/045007`, doi: 10.1088/0266-5611/31/4/045007.

CURRICULUM VITAE

Name SURNAME: Ahmet Caner GÜL

EDUCATION:

- **B.Sc.:** 2022, Yıldız Technical University, Faculty of Electrical and Electronics Engineering, Electronics and Communications Engineering
- **M.Sc.:** 2025, Istanbul Technical University, Faculty of Electrical and Electronics Engineering, Telecommunications Engineering

PROFESSIONAL EXPERIENCE AND REWARDS:

- 2022-... Research Assistant at Istanbul Technical University

PUBLICATIONS AND PRESENTATIONS ON THE THESIS:

- **GÜL A.C.,** International Graduate Research Symposium (IGRS'24), Istanbul. Poster presentation was held

OTHER PUBLICATIONS AND PRESENTATIONS:

- **A. C. Gül**, M. N. Akıncı and S. Doğu, "Millimeter-Wave Channel Modeling In Rural Areas," 2023 10th International Conference on Wireless Networks and Mobile Communications (WINCOM), Istanbul, Turkiye, 2023, pp. 1-4, doi: 10.1109/WINCOM59760.2023.10323002.
- E. S. Ahrazoglu, **A. C. Gul**, M. N. Akinci, I. Altunbas and E. Erdogan, "An Improved Pointing Error Model for mmWave and THz Links: Antenna and Array Design Impact," in IEEE Communications Letters, doi: 10.1109/LCOMM.2025.3529519.